Geophysical Prospecting, 2001, **49**, 523–539

The seismic response to overpressure: a modelling study based on laboratory, well and seismic data

José M. Carcione and Umberta Tinivella*

Istituto Nazionale di Oceanografia e di Geofisica Sperimentale, Osservatorio Geofisico Sperimentale, Borgo Grotta Gigante 42C, 34010 Sgonico (Trieste), Italy

Received January 2000, revision accepted March 2001

ABSTRACT

We investigate the seismic detectability of an overpressured reservoir in the North Sea by computing synthetic seismograms for different pore-pressure conditions. The modelling procedure requires the construction of a geological model from seismic, well and laboratory data. Seismic inversion and AVO techniques are used to obtain the P-wave velocity with higher reliability than conventional velocity analysis. From laboratory experiments, we obtain the wave velocities of the reservoir units versus confining and pore pressures. Laboratory experiments yield an estimate of the relationship between wave velocities and effective pressure under *in situ* conditions. These measurements provide the basis for calibrating the pressure model. Overpressures are caused by different mechanisms. We do not consider processes such as gas generation and diagenesis, which imply changes in phase composition, but focus on the effects of pure pore-pressure variations. The results indicate that changes in pore pressure can be detected with seismic methods under circumstances such as those of moderately deep North Sea reservoirs.

INTRODUCTION

Drilling of deep gas resources is hampered by the high risk associated with unexpected overpressure zones. Knowledge of pore pressure obtained using seismic data from, for instance, seismic-while-drilling techniques (Seisbit®, DBSeis®, Tomex®) will help in planning the drilling process so as to control potentially dangerous abnormal pressures.

In general, prediction of overpressure has been based on conventional velocity analysis (e.g. Bilgeri and Ademeno 1982) and empirical models relating pore pressure to seismic properties. Recently, Louis and Asad (1994) used a modelling technique to analyse the amplitude variations with offset (AVO) of pressure seals, and Pigott and Tadepalli (1996) estimated porosities and pore pressures in clastic rocks using AVO methods. Acoustic synthetic seismograms based on well logs showed that a strong AVO effect is associated with steep pressure and velocity gradients.

*E-mail: utinivella@ogs.trieste.it

We study the seismic visibility of overpressure using seismic, well and laboratory data. The analysis is intended to provide a procedure for overpressure detection from seismic data. We consider an area in the North Sea sedimentary basin. This basin is 170–200 km wide and represents a fault-bounded north-trending zone of extended crust, flanked by the mainland of western Norway and the Shetland Platform. The area is characterized by large normal faults with north, northeast and northwest orientations which define tilted blocks. Those flanking the Viking Graben are shown in Fig. 1. Jurassic and older sediments are present in the well used for this study. The main reason for selecting this area is the fact that high overpressure compartments were encountered during drilling, and that even higher overpressures are expected in future wells, down flank, towards the central Viking Graben. The well under study is an exploration well drilled to a total depth of 5149 mRKB (4767.4 mTVD) to test the hydrocarbon potential of the Jurassic Brent Group, which was encountered at about 3300 m depth. Figure 2 shows

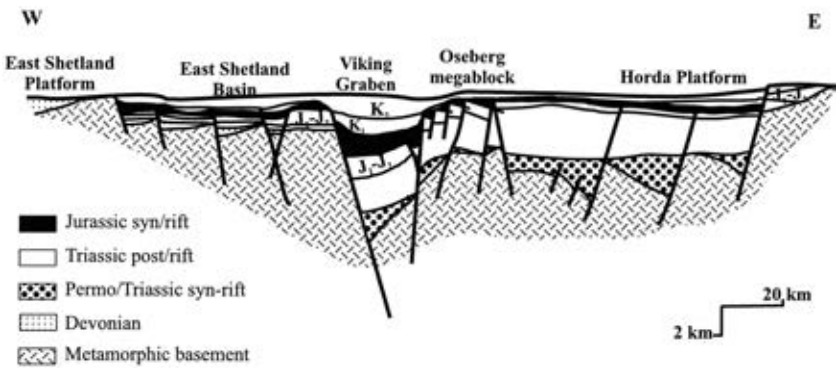

Figure 1 Cross-section showing the relationship between Jurassic and Permo-Triassic major fault-blocks and associated faults across the central segment of the North Sea at the end of the Cretaceous (from Færseth 1998). Cretaceous sediments (K_1 and K_2) represent infilling of remnant topography following Jurassic extension, J_1: Lower Jurassic, J_2: Middle Jurassic. The Viking Graben and its eastern margin show the interference of E- and W-dipping faults of Permo-Triassic and Jurassic origin, respectively.

a detail of the Brent Group and a synthetic seismogram computed from the sonic log. The well includes reservoir rocks of the Tarbert, Ness and Ore Formations. The Tarbert sands are the target of the present modelling study.

The investigation proceeds as follows. From seismic and well-logging data, we obtain a geological model of the well area. We use seismic inversion, AVO and prestack depth migration for seismic imaging, while the higher resolution of well-log data is used to define the geological features of the target formation. In addition, experiments performed on cores over the Tarbert sands from a nearby well yield the acoustic properties as a function of confining and pore pressure, under *in situ* conditions. These data and a suitable model for relating pore pressure to seismic properties enable us to compute synthetic seismograms and investigate the

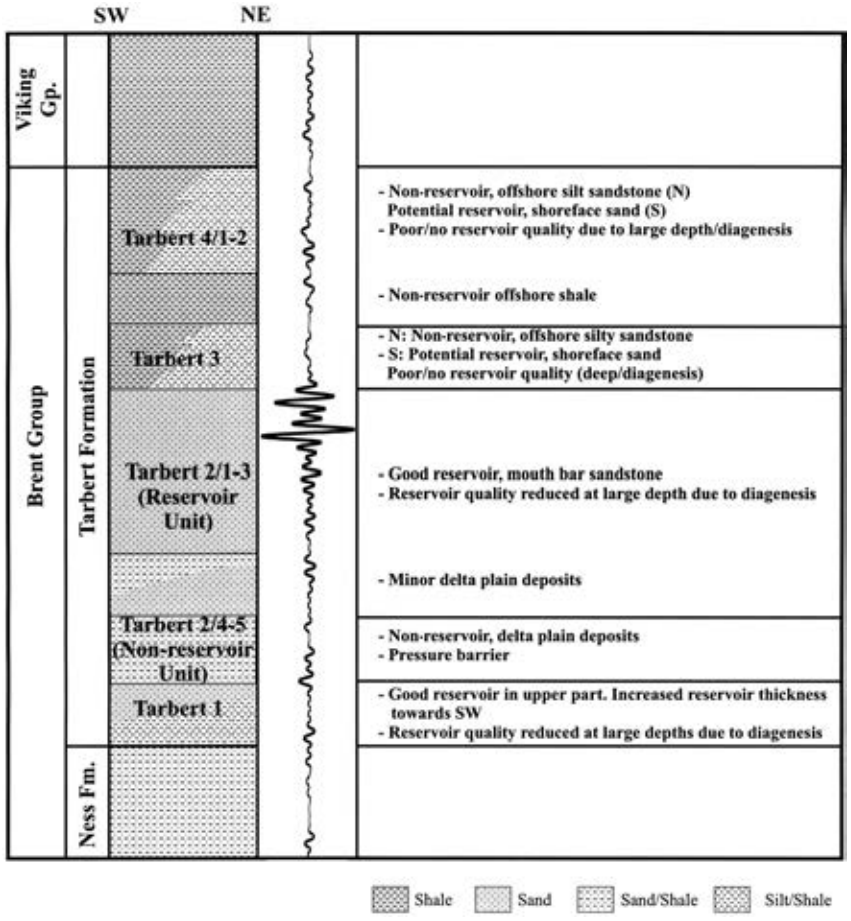

Figure 2 Zonation of the Tarbert Formation and a synthetic seismogram calculated from the sonic log (block 30/8).

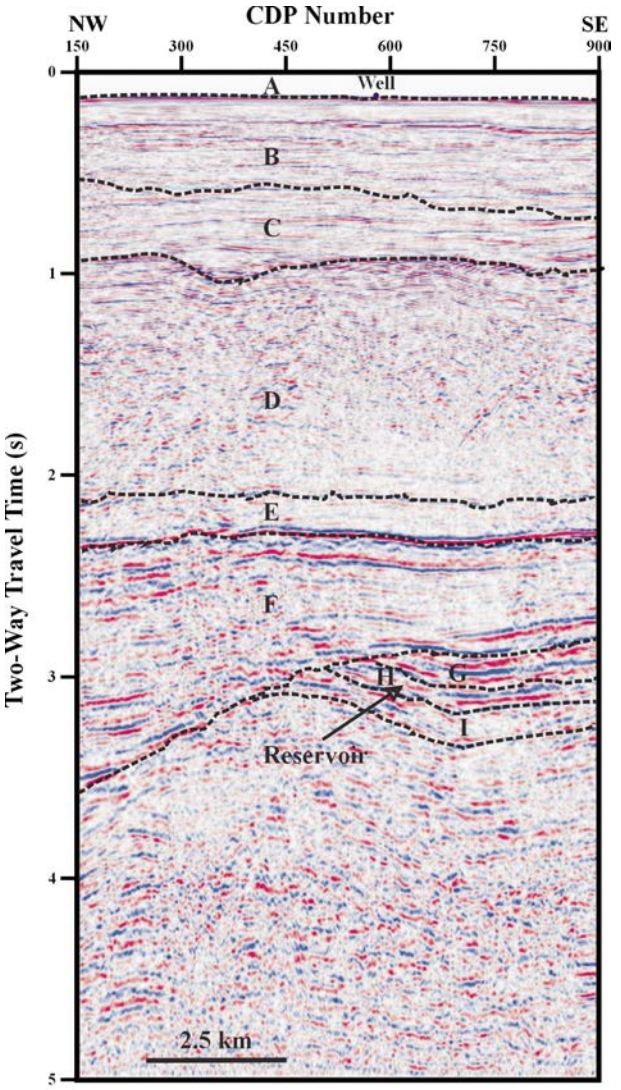

Figure 3 Stacked time-section for line SH9502-402.

seismic visibility of overpressure. This work is part of the modelling work-package for the European Union project 'Detection of overpressure zones with seismic and well data' (ODS), and as such, we make use of data provided by the different partners.

THE GEOLOGICAL MODEL

The location of the 2D seismic line SH9502-402, crossing well 30/8-1S, is approximately 165 km west of Bergen (Norway). The data were acquired using a 6 km streamer length, with a shot spacing of 25 m, a trace interval of 12.5 m and a sampling rate of 2 ms. The standard processing sequence applied to the data includes common-depth-point sorting, correction for geometrical spreading, low-cut filtering (to remove low-frequency noise), trace muting, and suppression of multiples. We consider a maximum offset of 3.2 km, since larger offsets present a very low signal-to-noise ratio. This represents a maximum angle of incidence of about 25° at the target level. The conventional stacked section, with a multiplicity of 60, is shown in Fig. 3.

The first version of the P-wave velocity model is obtained from the stacking velocities (Fig. 4, model 1). This model has relatively low resolution and is not suitable for seismic modelling analysis. A detailed interpretation of the existing 3D seismic data set in the study area, performed by one of the partners of the ODS project, provides a suitable geological model. Cretaceous and younger sequences are largely unfaulted and do not require additional interpretation, other than the usual standard procedure. The geological modelling procedure for the structurally more complex Jurassic sequences involved the generation of a seismic-coherence volume to define the main reservoir units and the associated minor faulting. The model is shown in Fig. 5 (model 2). A detailed interpretation of the target area (Fig. 6)

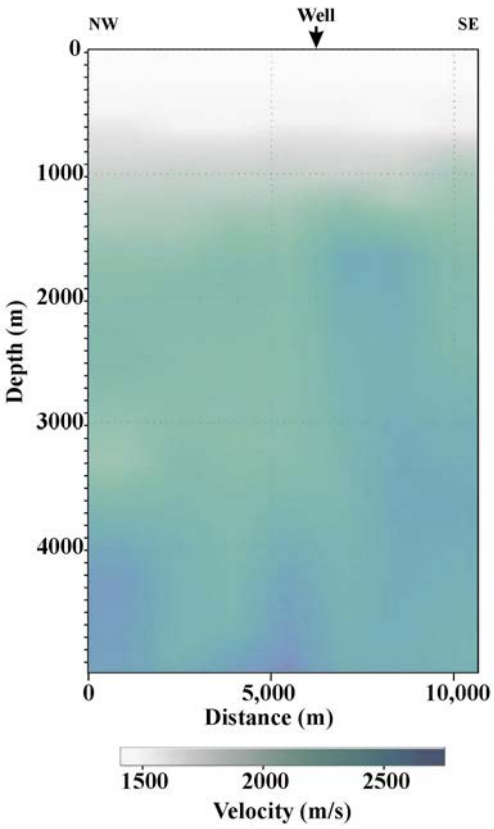

Figure 4 Geological model obtained from a conventional velocity analysis of seismic line SH9502-402 (model 1).

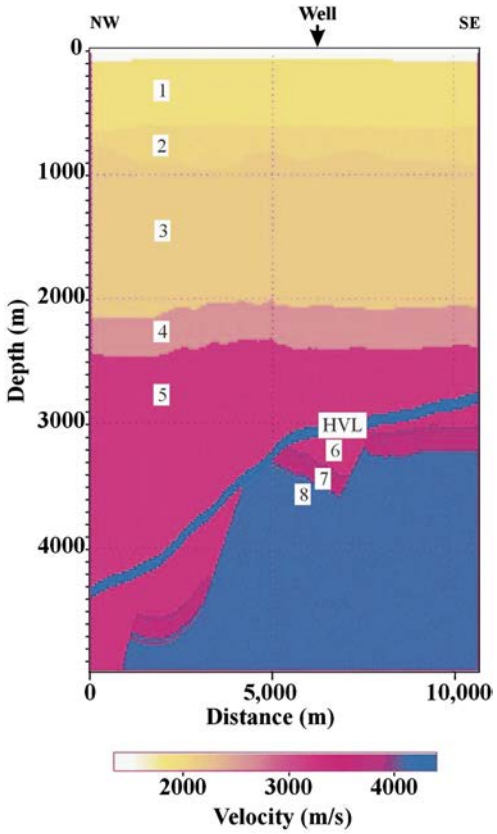

Figure 5 Geological model obtained from 3D seismic data and *a priori* geological information around well 30/8-1S. The modelling procedure involved the generation of a seismic-coherence volume to define the main reservoir units and the incorporation of fault-data of the study area (model 2).

is performed by including well-logging information (sonic and density logs, Fig. 7). The main geological structures are: a shallow low-velocity unit below the sea-floor (1), the Utsira Formation (2), a diapiric sequence (Hordaland Group) (3), the Balder Formation (4), the Cretaceous formations (5), the Viking Group (6) and the Brent Group, i.e. the Jurassic reservoir (7) and the Ness Formation (8). The Jurassic sequence includes four main units of the Tarbert Formation: Tarbert-4, Tarbert-3 (the top of the Brent Formation), Tarbert-2 (the reservoir) and Tarbert-1. On the basis of well-logging data, we include a high-velocity layer above the base of the Cretaceous (HVL), two layers in Tarbert-4 and four layers in the reservoir sands, three of which are very thin compared with the seismic wavelength (Kallweit and Wood 1982). In this case, Backus averaging (Backus 1962) is used to obtain the velocity field at the levels of seismic resolution. No lateral velocity variations are assumed in this interpretation.

In order to obtain a model with lateral velocity variations, we use the seismic inversion algorithm of the GeoDepth© software package (Paradigm Geophysical). Firstly, we interpret the stacked section by picking the main reflectors (see Fig. 3). These are the sea-floor (A), a shallow event (B), the top of the Utsira Formation (C), the top of the diapiric sequence (D), the top of the Balder Formation (E), the base and top of the Cretaceous (F), and three events in the Jurassic sequence (G, H and I). On the basis of these picks, the algorithm identifies the events in the prestack domain using coherence analysis. The velocity analysis provides the initial model for the inversion algorithm. This uses ray tracing to compute the moveout curves, and we choose the maximum semblance between data and predictions. This process is performed within a time window around the common midpoints (CMPs) predicted by the ray-tracing algorithm. Next, a depth section is generated using the interval velocities obtained with the inversion technique. Finally, the model is refined by using the horizon-based global-depth tomography algorithm, using depth delays. These delays give information about the residual error in moveout after prestack migration is applied to the data. This information is used to flatten the gathers. The degree of non-flatness yields a qualitative estimation of the error in the determination of the model. The tomographic algorithm uses these non-flatness estimates and finds an updated model with minimum error. The input to this process is the above-mentioned depth model and the conventional depth model obtained from velocity analysis. The final updated model obtained with the GeoDepth© package is shown in Fig. 8 (model 3). The main differences compared with the model shown in Fig. 5 are the presence of lateral velocity variations and the lack of the detailed features

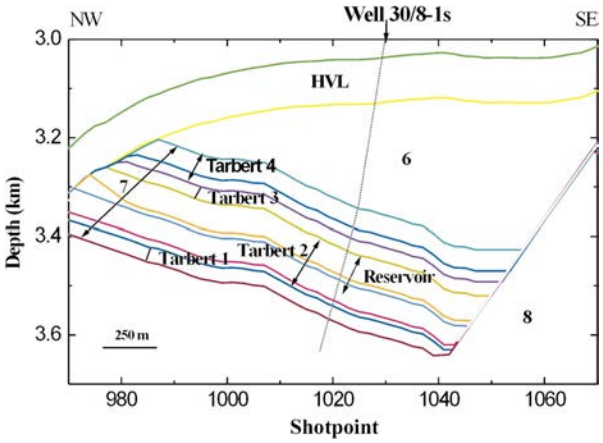

Figure 6 Interpretation of the reservoir units, using seismic, geological and well-logging (sonic- and density-log) information.

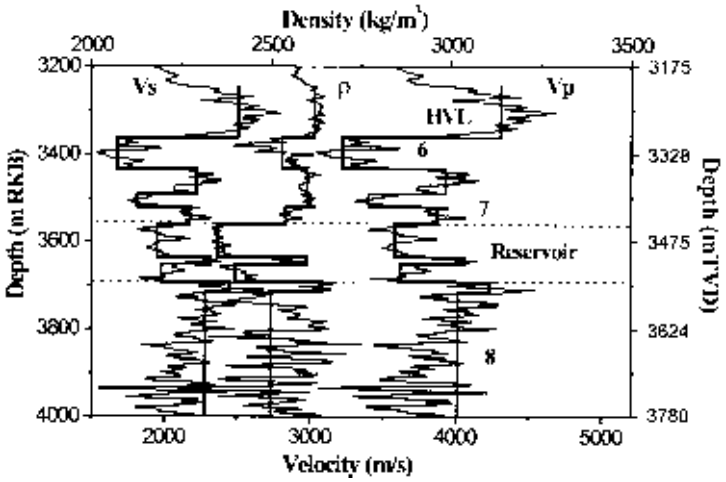

Figure 7 Sonic and density logs in well 30/8-1S. The S-wave log is obtained from the P-wave log by using the empirical relationship (1).

of the Brent Group. Figure 9 shows the P-wave velocity profile at the well location, corresponding to model 1 (dotted line), model 2 (thick broken line) and model 3 (thin broken line). The velocities obtained with conventional velocity analysis agree with the log velocities at shallow depths but differ for deep layers (Stewart, Huddleston and Tan 1984).

In order to test the velocity models we perform 2D prestack depth migration for each model, using the Seismic Unix software (a public-domain package available from Colorado School of Mines). The migrated sections are shown in Figs 10(a) (model 1), 10(b) (model 2) and 10(c) (model 3). Figure 10(d) shows a detail of the interpretation around the target formation. Model 1 is not suitable for obtaining good imaging of the structures. Model 3 is the best (mainly in the target zone, between 3.1 and 3.7 km depth) since lateral velocity variations are taken into account. The events indicated with dots in Fig. 10(d) are multiples. The broken lines correspond to reflections and the continuous lines to the main fault near the well. These events cannot be appreciated in the stacked unmigrated section (Fig. 3).

Table 1 shows the elastic properties which result from the interpretation and well-log information. The shear-wave velocity for layers 2–8 is given by

$$V_S[\mathrm{m/s}] = -792 + 0.765\, V_P[\mathrm{m/s}], \qquad (1)$$

where V_P is the P-wave velocity. This empirical equation is obtained by integrating the information from nearby wells, where logging measurements of shear-wave velocity were available. This relationship holds for brine-filled clastic rocks. The other properties are the density ρ, the P-wave and S-wave acoustic impedances I_P and I_S, respectively, and Poisson's ratio σ.

Amplitude variations with offset (AVO) analysis

AVO analysis is performed to obtain more information about the elastic properties, in particular about the shear-wave velocity of the target formation. We use two approaches: (i) the GeoDepth© algorithm and (ii) a least-squares algorithm.

Figure 11(a) shows a CMP gather at the well location. The top of the reservoir is indicated by an arrow in Fig. 3. This event corresponds to the interface Tarbert-3/Tarbert-2 (see Table 1). The AVO trend is shown in Fig. 11(b), where the open circles mark relative minimum amplitudes of the event picked in the time domain and the continuous line is the best-fit curve. We consider the minimum of the event, because there is a velocity inversion at the interface. The GeoDepth© algorithm, based on the linearization of Zoeppritz's equations, requires the following processing sequence: geometrical-spreading correction, surface-consistent scaling, correction for source and receiver directivities, correction for source and receiver array patterns, and attenuation compensation. We assume an average quality factor of 150 in view of the nature of the formations (Schön 1996). After applying this model-based conditioning to the data, we analyse the variations in the amplitude versus angle of incidence and obtain additional sections for various elastic parameters (P- and S-wave velocity and impedance reflectivities, fluid factor, etc.). The relationship between offset x and angle of incidence θ is calculated using the approximation

$$x = \frac{\sin(\theta) V_{\mathrm{rms}}^2 t(x)}{V_P},$$

where V_P is the vertical P-wave velocity of the upper layer, V_{rms} is the root-mean-square velocity and $t(x)$ is the time at offset x (Walden 1991). The analysis indicates that

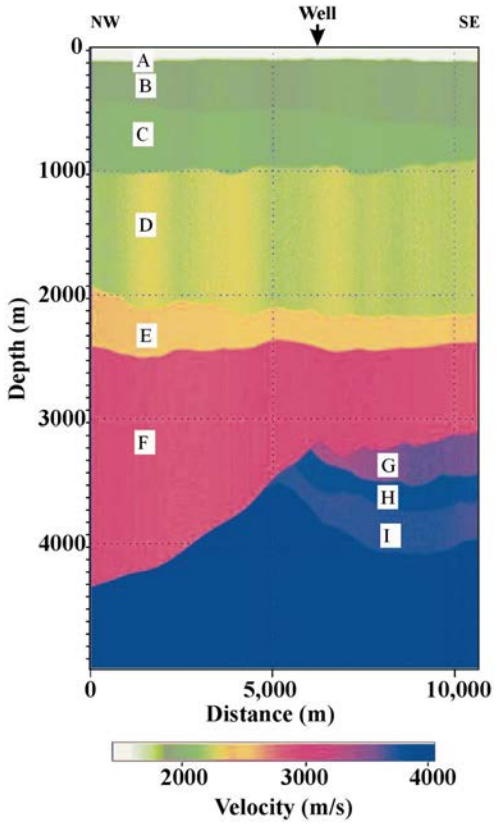

Figure 8 Geological velocity model obtained from the interpretation of seismic line SH9502-402 with the GeoDepth© software package (model 3).

the impedance reflectivities are more negative than the velocity reflectivities at the Tarbert-2 units (P-wave impedance reflectivity ≈ -0.077, P-wave velocity reflectivity ≈ -0.037), in agreement with the well-log data (see Fig. 7 and Table 1).

The second AVO algorithm can be summarized as follows: (i) selection and picking of reflectors in the CMP gather, (ii) frequency and velocity analysis, (iii) extraction of amplitudes versus offset and (iv) a least-squares inversion to obtain the acoustic properties by fitting the data to the exact theoretical reflection coefficient. We identify the top of the reservoir (Fig. 3) and pick the events in the CMP gather (Fig. 11). A frequency analysis gives a dominant frequency of 25 Hz. After applying geometrical spreading, attenuation (quality factor equal to 150) and overburden corrections, we obtain the normalized reflection coefficients. They are normalized with respect to the zero-offset reflection coefficient computed from the well-log data. We assume an isotropic and viscoelastic rheological equation, for which it is necessary to determine six acoustic properties: the P-wave velocity V_P, the shear-wave velocity V_S and the density ρ, for both the lower and upper media. We then minimize, in a least-squares sense, the difference between the reflection coefficient obtained from the seismic data and the theoretical reflection coefficient (Carcione 1997). We assume P-wave (S-wave) quality factors of 150 (100) and 30 (20) for the upper and lower layers (Schön 1996), respectively (in fact, attenuation has a limited influence on the offsets under consideration (Carcione, Helle and Zhao 1998)). Table 2 shows the best fit of the reflectivities using approach (ii), compared with those obtained from the well data, where V_S is given by equation (1) without taking the presence of gas into account (see also Fig. 7). The values are negative since the wave velocities and density of Tarbert-3 are greater than the wave velocities of Tarbert-2 (see Table 1). The main difference is in the shear-wave velocity, which we attribute to the presence of gas in Tarbert-2/1. The original Poisson's ratio of the Tarbert-2/1 to Tarbert-2/3 units is approximately 0.29. The AVO analysis implies a Poisson's ratio of 0.25, which is consistent with the presence of gas in the pore space (Khazanehdari, McCann and Sothcott 1998, paper presented at Conference on Pressure Regimes in Sedimentary Basins and their Prediction, Del Lago resort, Lake Conroe, Texas, USA). Therefore, the shear-wave velocity for the Tarbert-2 units is calculated using a Poisson's ratio of 0.25.

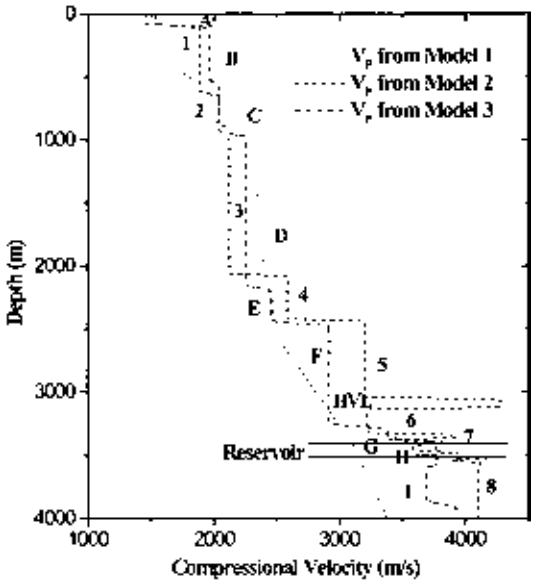

Figure 9 P-wave velocity profiles at the well location, corresponding to models 1, 2 and 3.

PRESSURE MODEL

First, we introduce some useful definitions of the different pressures considered in this work. *Pore pressure*, also known as formation pressure, is the *in situ* pressure of the fluids in the pores. The pore pressure is equal to the *hydrostatic pressure* when the pore fluids only support the weight of the overlying pore fluids (mainly brine). The *lithostatic* or *confining pressure* is due to the weight of overlying sediments, including the pore fluids. In the absence of any state of stress in the rock, the pore pressure attains lithostatic pressure and the fluids support all the weight. However, fractures perpendicular to the minimum compressive stress direction appear for a given pore pressure, typically 70–90% of the confining pressure. In this case, the fluid escapes from the pores and pore pressure decreases. A rock is said to be overpressured when its pore pressure is significantly greater than the hydrostatic pressure. The difference between pore pressure and hydrostatic pressure is called *differential pressure*. Acoustic and transport properties of rocks generally depend on *effective pressure*, a linear combination of pore and confining pressures (see equation (2)). Various physical processes cause anomalous pressures on an underground fluid. The most common causes of overpressure are thermal expansion of water, compaction disequilibrium and cracking, i.e. oil-to-gas conversion (Mann and Mackenzie 1990; Luo and Vasseur 1994).

In the following analysis we compute the variations in pore and fluid volume, which allow the calculation of the rock porosity and saturations as a function of pore pressure, the independent variable. These variations take place at nearly constant confining pressure (i.e. constant depth) and temperature. The changes are due solely to the compressibility effect, since at nearly constant temperature, thermal effects can be neglected. The reference state, for which all the properties are known, is the hydrostatic state. We consider constant composition within each phase, since the aim is to study variations due to pure pore-pressure effects rather than changes due to variations in material composition. A pressure model for variable composition was given by Berg and Gangi (1999), who calculated the excess pore pressure as a function of the fraction of kerogen converted to oil and the fraction of oil converted to gas. This model can easily be incorporated into the present theory.

We assume a closed rock unit at a fixed depth z and temperature T, representing a pressure compartment, which is characterized by an effective seal that prevents pressure equilibration to normal hydrostatic pressure (Bradley and Powley 1994). The lithostatic pressure for an average sediment density $\bar{\rho}$ is equal to $p_c = \bar{\rho} g z$, where g is the

Table 1 Material properties of the North Sea model

Layer	Medium	dbsf (m)	V_P (m/s)	V_S (m/s)	ρ (kg/m^3)	I_P (kg/m^{2}s)	I_S (kg/m^{2}s)	σ
0	Sea-water	0	1464	0	1040	1.464	0	0.5
1	Shallow layer	534	1890	750	1800	3.402	1.350	0.41
2	Utsira Formation	786	2030	762	1800	3.654	1.372	0.42
3	Diapiric sequence	1978	2121	832	2027	4.300	1.686	0.41
4	Balder Formation	2328	2582	1185	2271	5.864	2.691	0.37
5	Cretaceous	2945	3206	1662	2511	8.050	4.173	0.32
HVL	Cretaceous	3036	4253	2457	2626	11.168	6.452	0.25
6	Viking Group	3230	3266	1699	2528	8.256	4.295	0.31
7	Tarbert-4/1	3273	3894	2184	2595	10.105	5.667	0.27
7	Tarbert-4/2	3295	3472	1862	2601	9.031	4.843	0.30
7	Tarbert-3	3324	3876	2171	2558	9.915	5.553	0.27
7	Tarbert-2/1	3380	3601	1960	2362	8.506	4.629	0.29
7	Tarbert-2/2	3391	3816	2117	2502	9.548	5.297	0.28
7	Tarbert-2/3	3420	3623	1954	2416	8.753	4.721	0.29
7	Tarbert-2/4	3438	4140	2375	2640	10.930	6.275	0.25
7	Tarbert-2/5	3450	3965	2210	2457	9.742	5.430	0.27
7	Tarbert-1	3480	4124	2365	2534	10.450	5.993	0.25
8	Ness Formation	—	4101	2083	2538	10.408	5.287	0.32

dbsf, depth of base of group/formation/member below the sea-floor.

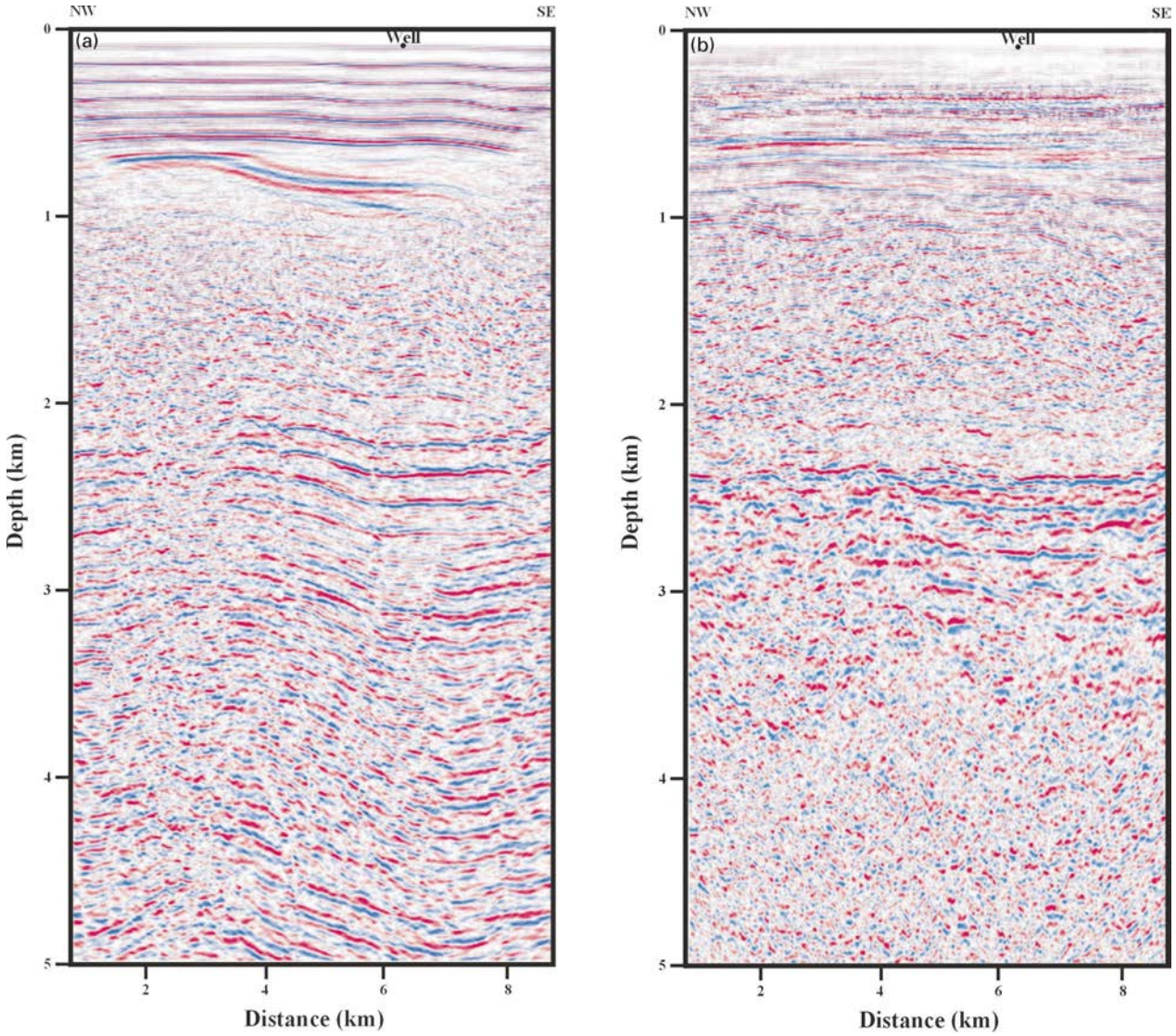

Figure 10 Prestack depth migration of seismic line SH9502-402 obtained with (a) model 1, (b) model 2 and (c) model 3. The interpretation of the target is shown in (d). The broken lines correspond to reflections and the continuous lines to the main fault near the well.

acceleration of gravity. On the other hand, the normal hydrostatic pore pressure is approximately $p_H = \rho_w g z$, where ρ_w is the density of brine.

In general, seismic properties, such as wave velocity and attenuation, depend on effective pressure,

$$p_e = p_c - np, \tag{2}$$

where p_e, p_c and p are the effective, confining and pore pressures and $n \leq 1$ is the effective stress coefficient. Note that the effective pressure equals the confining pressure at zero pore pressure. It is found that $n \approx 1$ for static measurements of the compressibilities (Zimmerman, Somerton and King 1986), while n is approximately linearly dependent on the differential pressure $p_d = p_c - p$ for dynamic experiments (Gangi and Carlson 1996; Prasad and Manghnani 1997): $n = n_0 - n_1 p_d$, where n_0 and n_1 are constant coefficients. Using this equation, the effective pressure (2) can be written as

$$p_e = p_c - (n_0 - n_1 p_c)p - n_1 p^2. \tag{3}$$

We know the porosity and fluid saturations at the hydrostatic pressure, and want to compute these quantities at a pore pressure higher than the hydrostatic pressure. Assuming oil, gas and brine in the pore space, the volume

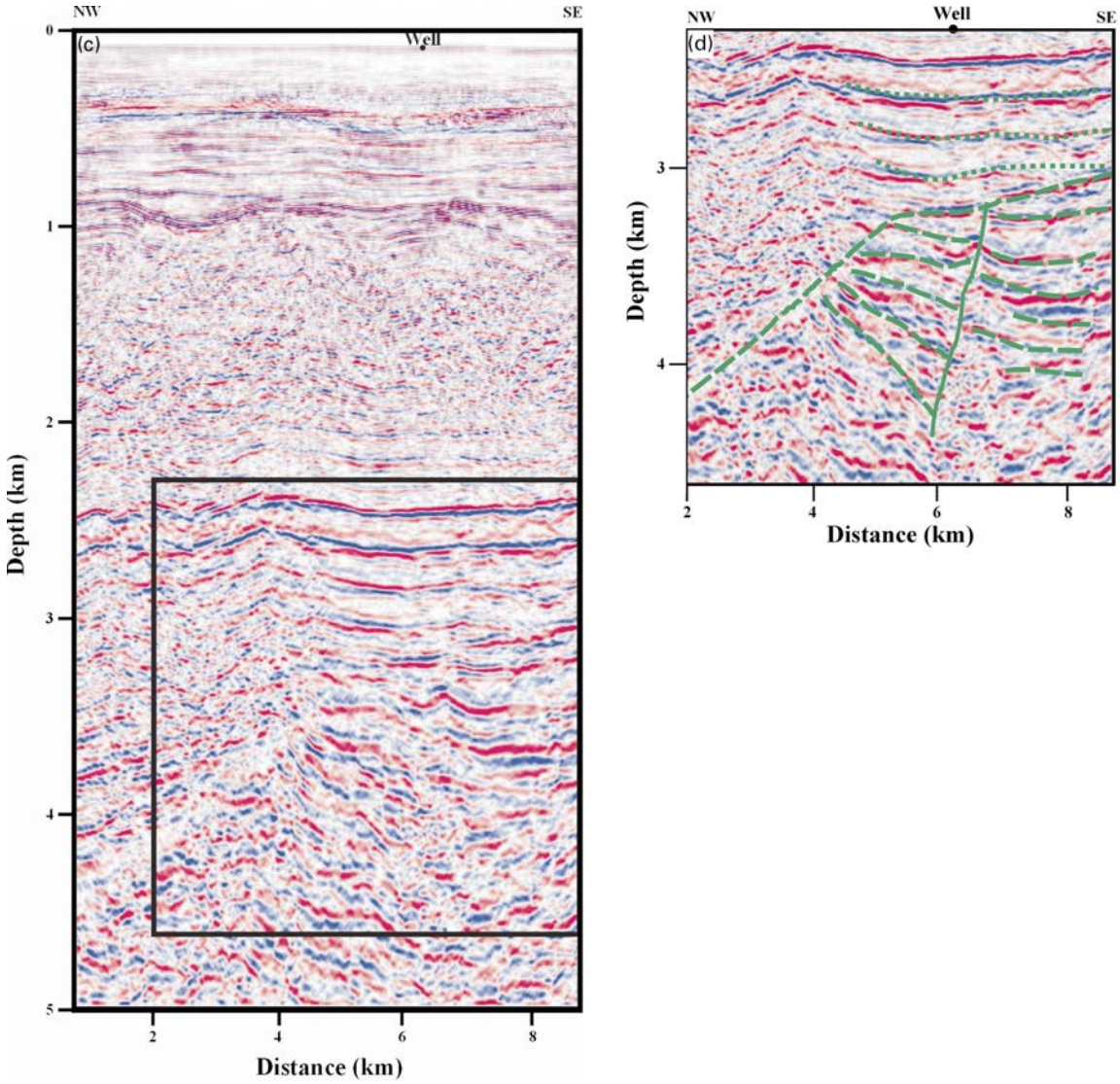

Figure 10 Continued

balance is $v_{\text{pore}} = v_{\text{o}} + v_{\text{g}} + v_{\text{w}}$, where v_{pore} is the pore volume, and v_{o}, v_{g} and v_{w} are the volumes of oil, gas and brine in the pore space, respectively. Since no mass (of the organics or the brine) leaves the pore space and the depth remains constant, the volume changes do not depend on mass and temperature, and we have

$$\mathrm{d}v_{\text{pore}} = \left(\frac{\partial v_{\text{pore}}}{\partial p_{\text{e}}}\right)\mathrm{d}p_{\text{e}} = \left(\frac{\partial v_{\text{o}}}{\partial p} + \frac{\partial v_{\text{g}}}{\partial p} + \frac{\partial v_{\text{w}}}{\partial p}\right)\mathrm{d}p_{\text{e}}, \tag{4}$$

with

$$c_{\text{p}} = -\frac{1}{v_{\text{pore}}}\frac{\mathrm{d}v_{\text{pore}}}{\mathrm{d}p_{\text{e}}}, \quad c_{\text{o}} = -\frac{1}{v_{\text{o}}}\frac{\mathrm{d}v_{\text{o}}}{\mathrm{d}p}, \quad c_{\text{g}} = -\frac{1}{v_{\text{g}}}\frac{\mathrm{d}v_{\text{g}}}{\mathrm{d}p},$$

$$c_{\text{w}} = -\frac{1}{v_{\text{w}}}\frac{\mathrm{d}v_{\text{w}}}{\mathrm{d}p}, \tag{5}$$

as the compressibilities for the pore space, oil, gas and brine. Note that the pore 'senses' the effective pressure, but the fluid 'senses' the pore pressure.

We assume that the compressibilities of the oil and brine are independent of pressure (it can be shown that the variations are less than 10% in the range of pore pressures investigated here (Batzle and Wang 1992)), and those of the gas and the rock depend on pressure. Moreover, we consider the following functional form for c_{p} as a function of

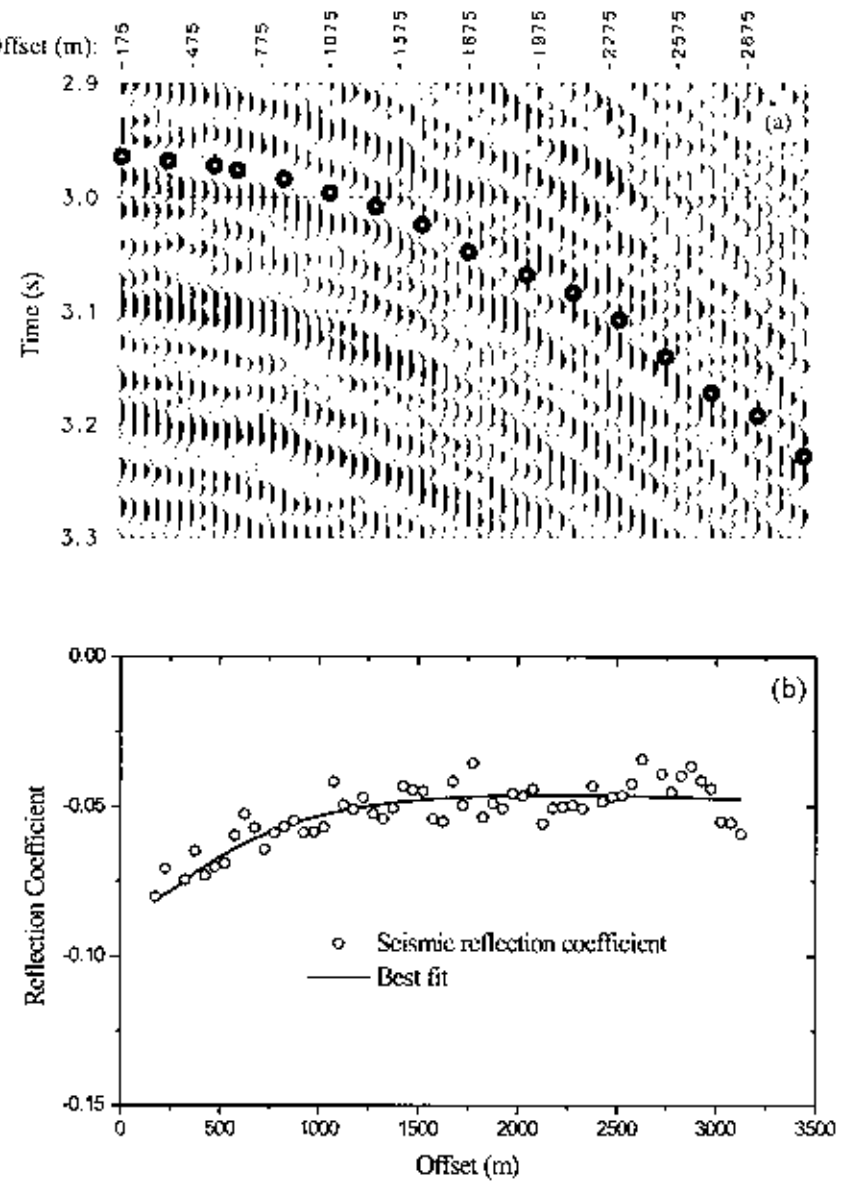

Figure 11 (a) CMP gather at the well location and (b) AVO trend of the top of the reservoir. The open circles indicate the reflection from the top of the reservoir (Brent Formation) and the open circles in (b) indicate the relative minimum amplitudes of the event picked in the time domain.

effective pressure:

$$c_{\mathrm{p}} = c_{\mathrm{p}}^{\infty} + \alpha p_{\mathrm{e}} + \beta \exp(-p_{\mathrm{e}}/p^{*}), \tag{6}$$

where c_{p}^{∞}, α, β and p^{*} are coefficients obtained by fitting the experimental data. Similar functional forms (6) are used to fit experimental data of pore compressibility (Zimmerman *et al.* 1986; Prasad and Manghnani 1997).

Table 2 Reflectivity at the top of the reservoir

	$\Delta V_{\mathrm{P}}/V_{\mathrm{P}}$	$\Delta V_{\mathrm{S}}/V_{\mathrm{S}}$	$\Delta\rho/\rho$
Well data	−0.0709	−0.0976	−0.0766
AVO analysis	−0.0708	−0.0451	−0.0793

Integration of equations (5) from the hydrostatic pressure $p_{\mathrm{i}} = p_{\mathrm{H}}$ to a given pore pressure p yields

$$v_{\mathrm{pore}}(p) = v_{\mathrm{pore,i}} \exp[E(\Delta p)], \tag{7}$$

$$v_{\mathrm{o}}(p) = v_{\mathrm{oi}} \exp(-c_{\mathrm{o}}\Delta p), \tag{8}$$

$$v_{\mathrm{g}}(p) = v_{\mathrm{gi}} \exp\left(-c_{\mathrm{g}} \int_{p_{\mathrm{i}}}^{p} c_{\mathrm{g}}(p)\, \mathrm{d}p\right) \tag{9}$$

and

$$v_{\mathrm{w}}(p) = v_{\mathrm{wi}} \exp(-c_{\mathrm{w}}\Delta p), \tag{10}$$

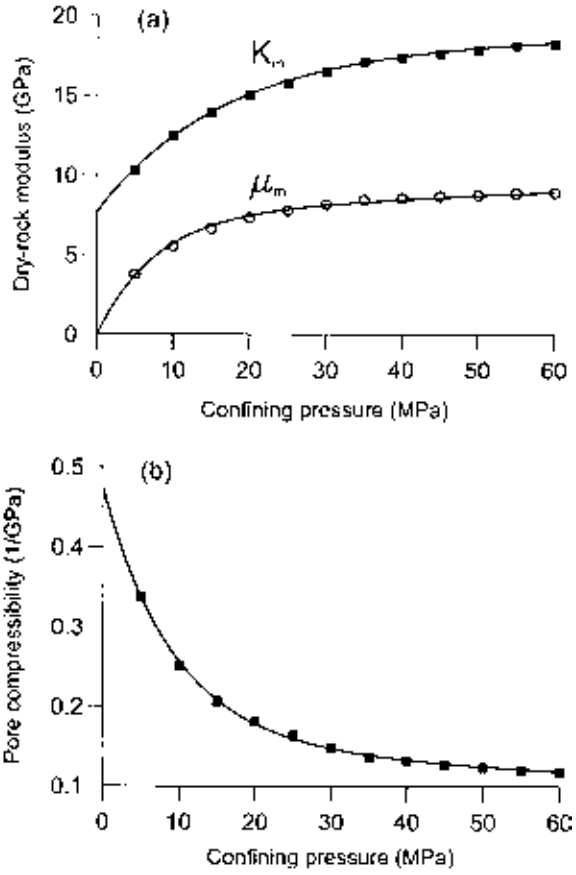

Figure 12 Regression fits to (a) dry-rock moduli K_m and μ_m and (b) pore compressibility c_p.

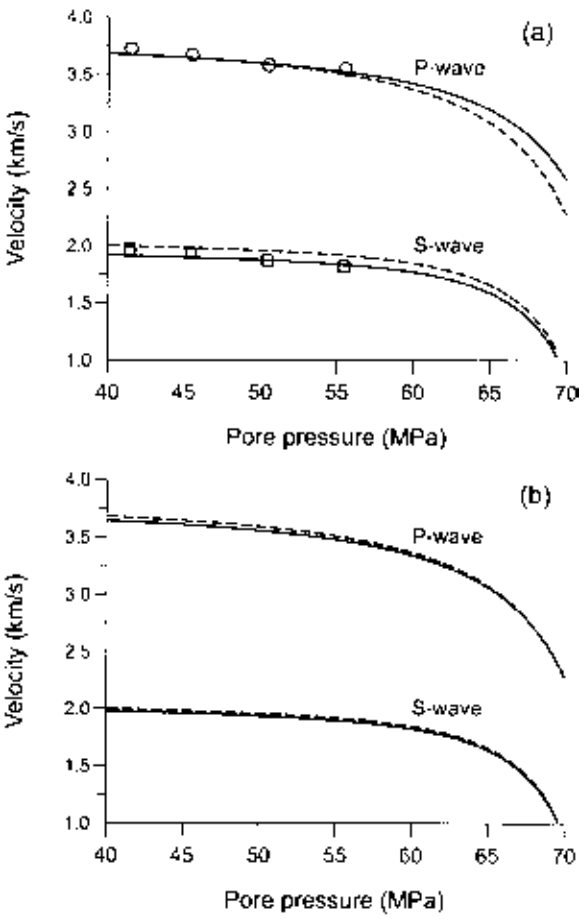

Figure 13 Compressional-wave velocity as a function of pore pressure for (a) full brine saturation and (b) partial saturation. In this case, the initial gas and brine saturations are $S_{gi} = 0.85$ and $S_{wi} = 0.15$, respectively. The confining pressure is 71.06 MPa. The dry-rock velocities are shown as broken lines. In this case, the horizontal axis corresponds to the confining pressure with zero pore pressure.

where $\Delta p = p - p_H$,

$$E(\Delta p) = -c_p^{\infty}\Delta p_e + \frac{1}{2}\alpha(p_e^2 - p_{ei}^2) + \beta p^* [\exp(-p_e/p^*) - \exp(-p_{ei}/p^*)],$$

and $\Delta p_e = p_e - p_{ei}$; the index i denotes the initial (hydrostatic) state and p_{ei} is the effective pressure at the initial state.

Using equations (7), (8)–(10), and since the initial saturations are

$$S_{wi} = v_{wi}/v_{pore,i}, \quad S_{oi} = v_{oi}/v_{pore,i}, \quad S_{gi} = v_{gi}/v_{pore,i}, \qquad (11)$$

the pore-volume balance equation becomes

$$\exp[E(\Delta p)] = S_{wi}\exp(-c_w\Delta p) + S_{oi}\exp(-c_o\Delta p) + S_{gi}\exp\left(-c_g\int_{p_i}^{p} c_g(p)\,dp\right). \qquad (12)$$

As the pore pressure changes from p_i to p, the pore volume changes from $v_{pore,i}$ to $v_{pore,i}\exp[E(\Delta p)]$. The saturations are equal to the corresponding volumes divided by the pore volume. Using equations (8) and (10), the requirement that $S_{gi} = 1 - S_{wi} - S_{oi}$ gives for the oil, brine and gas saturations,

$$S_o = S_{oi}\exp[-c_o\Delta p - E(\Delta p)], \qquad (13)$$

$$S_w = S_{wi}\exp[-c_w\Delta p - E(\Delta p)] \qquad (14)$$

and

$$S_g = 1 - S_w - S_o, \qquad (15)$$

respectively. On the other hand, the fluid proportions are

$$\phi_o = \phi S_o, \quad \phi_w = \phi S_w, \quad \phi_g = \phi S_g, \qquad (16)$$

where $\phi = v_{pore}/(v_{pore} + v_s)$ is the total porosity, with v_s denoting the volume of the solid part. This can be calculated

Table 3 Material properties for Tarbert-2 sandstone at 3.4 km depth and hydrostatic pore pressure

Grain	$\rho_s = 2650$ kg/m^3
	$K_s = 37$ GPa
	$\mu_s = 39$ GPa
Fluids	$\rho_g = 157$ kg/m^3
	$K_g = 92.6$ MPa
	$\eta_g = 0.02 \times 10^{-3}$ Pa s
	$\rho_w = 1045$ kg/m^3
	$K_w = 2.25$ GPa
	$\eta_w = 1.8 \times 10^{-3}$ Pa s
Matrix	$K_m = 17.95$ GPa
	$\mu_m = 8.77$ GPa
	$\phi = 0.189$
	$\kappa = 10^{-12}$ m^2
	$T = 2$

from the initial porosity ϕ_i (at hydrostatic pressure), since $\phi_i = v_{pore,i}/(v_{pore,i} + v_s)$. Thus, $v_s = v_{pore,i}(1/\phi_i - 1)$ and using (7), we obtain

$$\phi = \frac{\phi_i \exp[E(\Delta p)]}{1 - \phi_i\{1 - \exp[E(\Delta p)]\}}, \tag{17}$$

assuming incompressible grains in this calculation ($v_s \approx$ constant). Defining ϕ_s as the mineral matrix fraction, we have $\phi_s = 1 - \phi$. The pressure model can be refined by assuming the dependence on pressure and temperature of oil and brine compressibilities, and the influence of sodium chloride on brine properties. If one considers, for instance, the empirical formulae published by Batzle and Wang (1992), the solution can be obtained by numerical integration of the compressibilities.

Seismic velocities

The isothermal gas bulk modulus K_g and the gas compressibility $c_g = K_g^{-1}$ depend on pressure. The latter can be calculated from the van der Waals equation,

$$(p + a\rho_g^2)(1 - b\rho_g) = \rho_g RT, \tag{18}$$

where p is the gas pressure, ρ_g is the gas density, T is the absolute temperature and R is the gas constant. Moreover, a good approximation can be obtained using $a = 0.225\,\text{Pa}\,(\text{m}^3/\text{mole})^2 = 879.9\,\text{MPa}\,(\text{cm}^3/\text{g})^2$ and $b = 4.28 \times 10^{-5}\,\text{m}^3/\text{mole} = 2.675\,\text{cm}^3/\text{g}$ (one mole of methane, CH_4, corresponds to 16 g). Then,

$$c_g = \frac{1}{\rho_g}\frac{d\rho_g}{dp} = \left[\frac{\rho_g RT}{(1 - b\rho_g)^2} - 2a\rho_g^2\right]^{-1}. \tag{19}$$

In sandstones, the pore compressibility c_p is closely related to the bulk modulus of the matrix K_m (the compressibility c_p is denoted by C_{pp} by Zimmerman *et al.* (1986) and by $K_{\phi p}^{-1}$ by Mavko and Mukerji (1995), and K_m corresponds to C_{bc}^{-1} and K_{dry}^{-1}, respectively). Using the present notation, c_p can be expressed approximately as

$$c_p = \left(\frac{1}{K_m} - \frac{1}{K_s}\right)\frac{1}{\phi} - \frac{1}{K_s}, \tag{20}$$

where ϕ depends on the pore-pressure difference Δp at constant confining pressure. Since dry-rock wave velocities are practically frequency-independent, the seismic bulk moduli K_m and μ_m versus confining pressure can be obtained from laboratory measurements in dry samples. If V_{P0} and V_{S0} are the experimental dry-rock compressional- and shear-wave velocities, the moduli are given approximately by

$$K_m = (1 - \phi)\rho_s\left(V_{P0}^2 - \frac{4}{3}V_{S0}^2\right), \quad \mu_m = (1 - \phi)\rho_s V_{S0}^2, \tag{21}$$

where ρ_s is the grain density and ϕ is the porosity. We recall that K_m is the rock modulus at constant pore pressure, i.e. the case when the bulk modulus of the pore fluid is negligible compared with the frame bulk modulus, as, for example, air at room conditions (Mavko and Mukerji 1995).

The seismic velocities of the overpressured porous rock are

Table 4 Material properties of the reservoir units

Medium	V_P(Log) (m/s)	V_P(Lab) (m/s)	V_S(Log) (m/s)	V_S(AVO) (m/s)	V_S(Lab) (m/s)	ρ(Log) (kg/m^3)	ρ(Lab) (kg/m^3)
Tarbert-2/1	3601	3517	1960	2079	2045	2362	2202
Tarbert-2/2	3816	3517	2117	2203	2045	2502	2202
Tarbert-2/3	3623	3517	1954	2092	2045	2416	2202

AVO, from amplitude versus offset analysis (53 MPa); Lab, from laboratory experiments (53 MPa); Log, from well-log data (33.55 MPa).

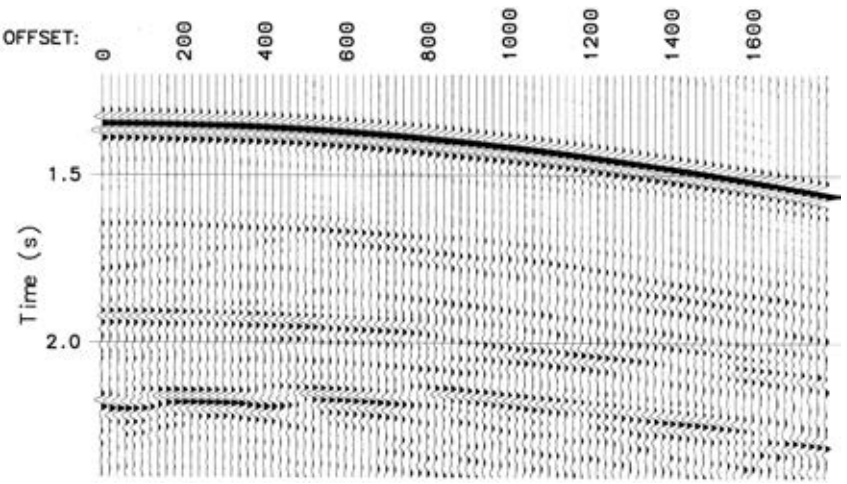

Figure 14 Synthetic RVSP (vertical component of the particle velocity) obtained with model 2 and a pore pressure of 53 MPa. The source (drill-bit) is located in the well at 3 km depth and the receivers are deployed at the sea-bottom (ocean-bottom cable). The bit is approximately 330 m above the top of the Brent Formation.

computed using Biot's theory of dynamic poroelasticity (Biot 1962; Carcione 1998), where fluid saturations and porosity versus pore pressure are given by equations (13), (14), (15) and (17). The velocities are given by (see Appendix)

$$V_{\mathrm{P}\pm} = \left[\mathrm{Re}\left(\frac{1}{V^*_{\mathrm{P}\pm}}\right)\right]^{-1}, \quad V_{\mathrm{S}} = \left[\mathrm{Re}\left(\frac{1}{V^*_{\mathrm{S}}}\right)\right]^{-1}, \tag{22}$$

where $V^*_{\mathrm{P}\pm}$ are the complex velocities of the fast (+) and slow (−) waves, V^*_{S} is the complex shear-wave velocity and Re denotes the real part.

SYNTHETIC SEISMOGRAMS FOR DIFFERENT PRESSURE CONDITIONS

Seismic properties of the reservoir sandstone versus pore pressure

The Tarbert-2 sandstone is located at a depth $z = 3.38$ km below the sea-floor (the water depth is approximately 100 m). From density-log data, the average sediment density from the surface to the Tarbert-2 sandstone is $\bar{\rho} = 2118\,\mathrm{kg/m^3}$, which gives a confining pressure of $p_{\mathrm{c}} = 71.06$ MPa. The hydrostatic pressure is $p_{\mathrm{H}} = 33.55$ MPa (assuming $\rho_{\mathrm{w}} = 1040\,\mathrm{kg/m^3}$). The well report indicates a temperature between 110°C and 120°C, which is consistent with a surface temperature $T_0 = 10$°C and a geothermal gradient $G = 30$°C/km (on the basis of the linear relationship $T = T_0 + Gz$). The pore pressure measured in the well is 53 MPa (530 bar).

The laboratory data are provided by the Institute of Sedimentology at Reading University. On the basis of these data and equations (21) for p_{c} ranging from 0 to 72 MPa, best-fit estimates of the dry-rock moduli versus confining pressure are

$$K_{\mathrm{m}}[\mathrm{GPa}] = 17.87 + 0.011 p_{\mathrm{c}}[\mathrm{MPa}] - 10.15\exp(-p_{\mathrm{c}}[\mathrm{MPa}]/16.51)$$

and

$$\mu_{\mathrm{m}}[\mathrm{GPa}] = 7.58 + 0.023 p_{\mathrm{c}}[\mathrm{MPa}] - 7.64\exp(-p_{\mathrm{c}}[\mathrm{MPa}]/7.77),$$

and c_{p} in MPa is given by equation (6), with $c_{\mathrm{p}}^{\infty} = 0.1483$, $\alpha = -0.0005$, $\beta = 0.3237$, $p^* = 9.56$. The pore compressibility c_{p} is obtained from equation (20) by assuming that the porosity is that at hydrostatic pore pressure (this approximation is supported by experimental data obtained by Domenico (1977) and Han, Nur and Morgan (1986)). The best-fit plots for K_{m} and μ_{m} (a) and c_{p} (b) versus pore pressure are illustrated in Fig. 12.

In order to obtain the moduli for different combinations of the confining and pore pressures we make the substitution $p_{\mathrm{c}} \rightarrow p_{\mathrm{e}} = p_{\mathrm{c}} - np$, where we assume, following Gangi and Carlson (1996), that n depends on differential pressure and is given by

$$n = n_0 - n_1 p_{\mathrm{d}}.$$

This relationship of n versus differential pressure is in good agreement with the experimental values corresponding to the compressional-wave velocity obtained by Christensen and Wang (1985) and Prasad and Manghnani (1997). Experimental evidence indicates that n is different for each physical property. A linear best-fit of the values provided by Reading University yields

bulk modulus and compressibility : $n_0 = 1$,

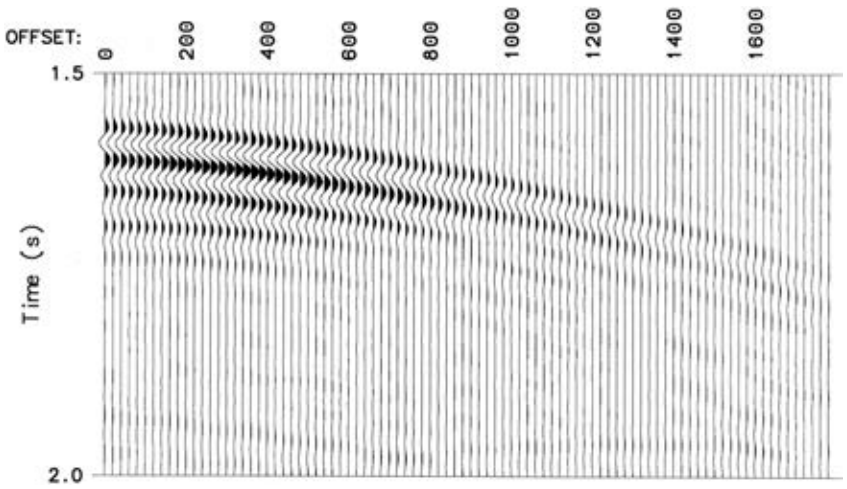

Figure 15 Difference between the 53 MPa and hydrostatic-pressure synthetic seismograms. The main reflection corresponds to the top of the reservoir.

$n_1 = 0.01\,\mathrm{MPa}^{-1}$

and

shear modulus : $\quad n_0 = 1, \quad n_1 = 0.012\,\mathrm{MPa}^{-1}$.

Table 3 indicates the properties for the Tarbert-2 sandstone. The gas properties, according to the petrophysical report of the well, correspond to a pressure of 53 MPa. They give a sound velocity of 768 m/s. The matrix properties correspond to those at the initial (hydrostatic) pore pressure. The brine density and bulk modulus are assumed to be pressure-independent.

Figure 13(a) shows the compressional-wave velocity versus pore pressure for a confining pressure $p_c = 71.06\,\mathrm{MPa}$ (continuous lines), compared with the experimental values provided by Reading University for full brine saturation ($S_{wi} = 1.$). They also provided the velocities for different confining and pore pressures. Knowing n, it is possible to obtain the velocities for different combinations of the pore and confining pressures, in particular for $p_c = 71.06\,\mathrm{MPa}$ and variable pore pressure. Each experimental point in Fig. 13(a) corresponds to a pore pressure p, that is a solution of the second-degree equation (3). The velocity decreases substantially with increasing pore pressure, mainly because of the opening of compliant cracks. This information is contained in the behaviour of the dry-rock moduli as a function of confining pressure.

In the following, we assume an initial gas saturation $S_{gi} = 0.85$ and brine saturation $S_{wi} = 0.15$, which are those given in the well report. Figure 13(b) shows the wave velocities versus pore pressure at a confining pressure of 71.06 MPa. The dry-rock velocities are shown as broken lines (in this case, the horizontal axis corresponds to the confining pressure with zero pore pressure). Because of the decrease in density, the S-wave velocity is higher than the S-wave velocity for full brine saturation (see Fig. 13a). The small difference between the dry-rock and wet-rock velocities in Fig. 13(b) indicates that in this case the presence of gas has not had a major effect on the velocities.

The properties of the reservoir layers obtained from seismic, well-log and laboratory data (one sample) are given in Table 4 for a pore pressure of 53 MPa, which was the pressure regime when the seismic data were acquired (although the well-log velocities should correspond, in principle, to the hydrostatic pressure 33.55 MPa because they are obtained from open-hole measurements). Since in this study we have both well and laboratory data, we assume that the properties of the reservoir are those obtained with laboratory data, as indicated in Table 4. The wave velocities

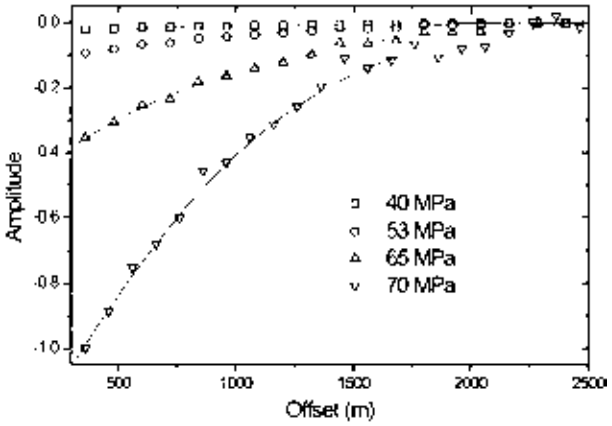

Figure 16 AVO trends of the first event in the difference seismograms, corresponding to different pore-pressure regimes. The continuous lines are best-fit regression curves.

of the dry rock, determined by laboratory measurements, give estimates of the pore compressibility and bulk moduli in the low-frequency (relaxed) regime. Since dissipation mechanisms are caused mainly by grain/fluid interactions, dry-rock velocities are approximately frequency-independent (Spencer 1981).

Synthetic seismograms

We compute 2D synthetic seismograms with the source located in the well at 3 km depth (see Fig. 6) and the receivers deployed at the sea-bottom (ocean-bottom cable (OBC)). The numerical experiment simulates a reverse vertical seismic profile (RVSP), using the drill-bit as a source. Note that to obtain real-data RVSP requires an autocorrelation of the drill-bit data with the pilot signal travelling through the drill-string (Aleotti *et al.* 1999). The synthetic seismograms are computed with a modelling algorithm based on the velocity–stress formulation of the isotropic-viscoelastic wave equation. The Fourier pseudospectral method is used to calculate the spatial derivatives and a fourth-order Runge-Kutta technique is used to obtain the wavefield recursively in time (Carcione 1992). The numerical mesh has 231×231 points with a grid spacing $D_X = D_Z = 20\,\text{m}$. The source is a Ricker-type wavelet with a dominant frequency of 25 Hz. We assume P-wave (S-wave) quality factors of 150 (100) for all the layers. Five synthetic seismograms have been computed, corresponding to different pore-pressure regimes in the reservoir: 33.55 MPa (hydrostatic pressure), 40 MPa, 53 MPa, 65 MPa and 70 MPa. The synthetic seismogram for a pore pressure of 53 MPa (measured pressure while drilling) is shown in Fig. 14. The first strong event is the direct wave, which masks the reflected event from the base of the Cretaceous. The reflection from the top of the reservoir is located between 1.6 s and 1.75 s. Figure 15 shows the difference between the 53 MPa and hydrostatic-pressure seismograms. Similar difference seismograms have been obtained for 40, 65 and 70 MPa. The AVO trends of the first event in these difference seismograms are shown in Fig. 16, where the continuous lines are best-fit regression curves. The behaviour is similar to that shown in Fig. 11(b), obtained from the real-data CMP gather. Strong and negative differential AVO effects are associated with high pore pressures, approaching the confining pressure. These effects are more important for near and medium offsets.

CONCLUSIONS

Seismic data and a suitable rock-acoustics model, relating the seismic properties to pore pressure, enable the determination of overpressure in advance of drilling. This modelling study shows the influence of high pore pressures on seismic velocities and amplitude variations with offset. The model relating pore pressure to seismic velocity requires calibration with laboratory measurements of wave velocities versus confining and pore pressures. Measurements of dry-rock moduli and pore compressibility versus confining pressure are essential for proper use of the Biot–Gassmann equations, since these moduli contain implicit microstructural information. In addition, experiments on saturated samples for different confining and pore pressures give the effective-stress coefficient, which enables the calculation of seismic properties versus effective pressure. On the other hand, seismic inversion and AVO techniques can be used to obtain wave velocities with higher reliability than conventional processing techniques, and well-log data are essential in order to provide a high-resolution geological model, appropriate for overpressure modelling studies. In the particular case of the North Sea reservoir investigated, strong and negative differential AVO effects are associated with overpressure. The effects are important at high pore pressures and near and medium offsets.

ACKNOWLEDGEMENTS

This work was supported by the European Union under the project 'Detection of overpressure zones with seismic and well data'. We thank our partners of the ODS project, Hans B. Helle, Clive McCann, John J. Walsh and Bill Martin, for their co-operation in making the data available. We are grateful to Zvi Koren and Dan Kosloff of Paradigm Geophysical for providing the GeoDepth© software.

REFERENCES

Aleotti L., Poletto F., Miranda F., Corubolo P., Abramo F. and Craglietto A. 1999. Seismic while-drilling technology: use and analysis of the drill-bit seismic source in cross-hole survey. *Geophysical Prospecting* **47**, 25–39.

Backus G.E. 1962. Long-wave elastic anisotropy produced by horizontal layering. *Journal of Geophysical Research* **67**, 4427–4440.

Batzle M. and Wang Z. 1992. Seismic properties of pore fluids. *Geophysics* **57**, 1396–1408.

Berg R.R. and Gangi A.F. 1999. Primary migration by oil-generation

microfracturing in low-permeability source rocks. Application to the Austin chalk, Texas. *AAPG Bulletin* **83**, 727–756.

Berryman J.G., Thigpen L. and Chin R.C.Y. 1988. Bulk elastic wave propagation in partially saturated porous solids. *Journal of the Acoustical Society of America* **84**, 360–373.

Bilgeri D. and Ademeno E.B. 1982. Predicting abnormally pressured sedimentary rocks. *Geophysical Prospecting* **30**, 608–621.

Biot M.A. 1962. Mechanics of deformation and acoustic propagation in porous media. *Journal of Applied Physics* **33**, 1482–1498.

Bradley J.S. and Powley D.E. 1994. Pressure compartments in sedimentary basins: a review. *AAPG Memoir* **61**, 3–26.

Carcione J.M. 1992. Modeling anelastic singular surface waves in the Earth. *Geophysics* **57**, 781–792.

Carcione J.M. 1997. Reflection and refraction of *qP-qS* plane shear waves at a plane boundary between viscoelastic transversely isotropic media. *Geophysical Journal International* **129**, 669–680.

Carcione J.M. 1998. Viscoelastic effective rheologies for modelling wave propagation in porous media. *Geophysical Prospecting* **46**, 249–270.

Carcione J.M., Helle H. and Zhao T. 1998. The effects of attenuation and anisotropy on reflection amplitude versus offset. *Geophysics* **63**, 1652–1658.

Christensen N.I. and Wang H.F. 1985. The influence of pore pressure and confining pressure on dynamic elastic properties of Berea sandstone. *Geophysics* **50**, 207–213.

Domenico S.N. 1977. Elastic properties of unconsolidated porous sand reservoirs. *Geophysics* **42**, 1339–1368.

Færseth R.B. 1996. Interaction of Permo-Triassic and Jurassic extensional fault-blocks during the development of the northern Sea. *Journal of the Geological Society, London* **153**, 931–944.

Gangi A.F. and Carlson R.L. 1996. An asperity-deformation model for effective pressure. *Tectonophysics* **256**, 241–251.

Han D.H., Nur A. and Morgan D. 1986. Effects of porosity and clay content on wave velocities in sandstones. *Geophysics* **51**, 2093–2107.

Kallweit R.S. and Wood L.C. 1982. The limits of resolution of zero-phase wavelets. *Geophysics* **47**, 1035–1046.

Louis J.N. and Asad A.M. 1994. Seismic amplitude versus offset (AVO) character of geopressured transition zones. *AAPG Memoir* **61**, 131–137.

Luo X. and Vasseur G. 1996. Geopressuring mechanism of organic matter cracking: numerical modeling. *AAPG Bulletin* **80**, 856–874.

Mann D.M. and Mackenzie A.S. 1990. Prediction of pore fluid pressures in sedimentary basins. *Marine and Petroleum Geology* **7**, 55–65.

Mavko G. and Mukerji T. 1995. Seismic pore space compressibility and Gassmann's relation. *Geophysics* **60**, 1743–1749.

Pigott J.D. and Tadepalli S.V. 1996. Direct determination of clastic reservoir porosity and pressure from AVO inversion. 66th SEG meeting, Denver, USA, Expanded Abstracts, 1759–1762.

Prasad M. and Manghnani M.H. 1997. Effects of pore and differential pressure on compressional wave velocity and quality factor in Berea and Michigan sandstones. *Geophysics* **62**, 1163–1176.

Schön J.H. 1996. *Physical Properties of Rocks. Fundamentals and Principles of Petrophysics*. Pergamon Press, Inc.

Spencer J.W., Jr. 1981. Stress relaxation at low frequencies in fluid-saturated rocks: attenuation and modulus dispersion. *Journal of Geophysical Research* **86**, 1803–1812.

Stewart R.R., Huddleston P.D. and Kan T.K. 1984. Seismic versus sonic velocities. *Geophysics* **49**, 1153–1168.

Walden A.T. 1991. Making AVO sections more robust. *Geophysical Prospecting* **39**, 915–942.

Zimmerman R.W., Somerton W.H. and King M.S. 1986. Compressibility of porous rocks. *Journal of Geophysical Research* **91**, 12765–12777.

APPENDIX

Seismic velocities of a porous medium saturated with hydrocarbons and brine

Biot's theory of dynamic poroelasticity is used to compute seismic velocities, where the pore fluid is a mixture of hydrocarbon and brine. The complex velocities of the fast (+ sign) and slow (− sign) compressional waves and the shear wave are given by (Biot 1962),

$$V^{*2}_{\mathrm{P}\pm} = \frac{A \pm \sqrt{A^2 - 4ME\rho_{\mathrm{c}}\rho'}}{2\rho_{\mathrm{c}}\rho'} \tag{A1}$$

and

$$V^{*2}_{\mathrm{S}} = \frac{\mu}{\rho_{\mathrm{c}}}, \tag{A2}$$

where

$$A = M(\rho - 2\alpha\rho_{\mathrm{f}}) + \rho'(E + \alpha^2 M),$$

$$\rho_{\mathrm{c}} = \rho - \rho_{\mathrm{f}}^2/\rho'$$

and

$$\rho' = \frac{T}{\phi}\rho_{\mathrm{f}} - \frac{\mathrm{i}}{2\pi f}\frac{\eta}{\kappa},$$

with f denoting the frequency and $i = \sqrt{-1}$. The sediment density is given by

$$\rho = (1 - \phi)\rho_{\mathrm{s}} + \phi\rho_{\mathrm{f}},$$

where ρ_{s} and ρ_{f} are the solid and fluid densities, respectively; T is the tortuosity, η is the fluid viscosity and κ is the permeability of the medium.

The elastic coefficients are given by

$$E = K_{\mathrm{m}} + \frac{4}{3}\mu_{\mathrm{m}}, \tag{A3}$$

$$M = \frac{K_s^2}{D - K_m}, \tag{A4}$$

$$D = K_s[1 + \phi(K_s K_f^{-1} - 1)], \tag{A5}$$

$$\alpha = 1 - \frac{K_m}{K_s}, \tag{A6}$$

with K_s being the bulk modulus of the solid grains and K_f the bulk modulus of the hydrocarbon/brine mixture. The stiffness E is the P-wave modulus of the dry skeleton, M is the elastic coupling modulus between the solid and the fluid and α is the poroelastic coefficient of effective stress.

The hydrocarbon/brine mixture behaves as a composite fluid with properties depending on the constants of the constituents and their relative concentrations. This problem has been analysed by Berryman, Thigpen and Chin (1988) and the results are given by the formulae

$$K_f = (S_o c_o + S_g c_g + S_w c_w)^{-1}, \tag{A7}$$

$$\rho_f = S_o \rho_o + S_g \rho_g + S_w \rho_w, \tag{A8}$$

where ρ_o is the density of oil, and

$$\eta_f = S_o \eta_o + S_g \eta_g + S_w \eta_w, \tag{A9}$$

where η_o, η_g and η_w are the viscosities of the oil, gas and brine, respectively. Equation (A9) is a good approximation for most values of the saturations.

The phase velocity $V_{P(S)}$ is equal to the angular frequency $\omega = 2\pi f$ divided by the real wavenumber. Then we have

$$V_{P\pm} = \left[\mathrm{Re}\left(\frac{1}{V^*_{P\pm}}\right)\right]^{-1}, \quad V_S = \left[\mathrm{Re}\left(\frac{1}{V^*_S}\right)\right]^{-1}, \tag{A10}$$

where Re denotes the real part.